MATERIALS CHEMISTRY FRONTIERS

RESEARCH ARTICLE

View Article Online
View Journal | View Issue

Cite this: *Mater. Chem. Front.*, 2025, **9**, 2730

3D printed C_3N_4-based structures for photo-, electro-chemical and piezoelectric applications†

Alessio Massaro, *[ab] Kiem Giap Nguyen, [c] David Vogelsang Suárez, [a] Artem Glukharev, [a] Chiara Ingrosso, [d] Marinella Striccoli, [d] Ahmet Can Kirlioglu,[a] Suela Kellici [c] and Vesna Middelkoop *[a]

Received 3rd April 2025,
Accepted 11th June 2025

DOI: 10.1039/d5qm00290g

rsc.li/frontiers-materials

In this study, we explored the use of two 3D printing techniques, direct ink writing (DIW) and digital light processing (DLP), as novel and flexible strategies to control the 3D geometry and morphology of functional materials. To demonstrate their potential, different types of carbon nitride (C_3N_4) were combined and successfully printed with various polymers, such as methylcellulose (MC) and polysulfone (PSF). C_3N_4 is a metal-free photoactive material, which has recently gained significant interest due to its attractive optoelectronic properties. The 3D printed C_3N_4-based composites were tested in typical potential applications for their photo-, piezo- and electrocatalytic activity. Tailored formulations and design strategies were devised for pollutant photo- and piezoelectric degradation as well as electrochemical sensing, showing the effect of the formulation on the performance of the 3D printed C_3N_4 polymer composites. The performance evaluations revealed promising results, complemented by the stability of the 3D printed geometries in organic solvents commonly used in chemical syntheses. Specifically, the DIW g-C_3N_4/PSF formulation showed the highest overall pollutant removal (71%), followed by the DLP g-C_3N_4-based formulations which showed high removal efficiencies (up to 63%) with a high level of piezoelectric degradation (up to 41%). In addition, Piezoresponse Force Microscopy (PFM) analysis of both the starting bulk g-C_3N_4 powder and DIW 3D printed bulk g-C_3N_4/MC composite revealed significant piezoelectric properties, broadening their potential applications.

1. Introduction

Due to their potential for innovative applications, semiconductor heterogeneous photocatalysis has attracted widespread attention. A primary objective is the development of highly efficient material for photocatalytic performance, offering stability and cost-effectiveness. Graphitic carbon nitride (g-C_3N_4), a metal-free polymer n-type semiconductor, has emerged as a promising candidate due to its distinctive electrical, optical, structural, catalytic and physiochemical properties, as well as its biocompatibility.[1–4] Since Wang *et al.* demonstrated the photocatalytic capability of g-C_3N_4 for H_2 and O_2 evolution in 2009,[5] g-C_3N_4-based materials have been increasingly explored as multifunctional nanoplatforms in a vast range of energy and environmental applications, including photocatalytic and electrochemical conversion,[6–9] electrochemical sensing, pollutant degradation,[10,11] CO_2 reduction,[7,12–14] hydrogen production,[7,12–14] piezoelectric catalysis,[15,16] and many other fields, due to its good chemical stability, corrosion resistance, optical properties, environmental friendliness and lower cost. Additionally, with a relatively narrow bandgap of 2.7 eV, g-C_3N_4 exhibits strong visible light absorption, further enhancing its potential as an ideal photocatalyst for various applications, including water splitting, pollutant degradation, and carbon dioxide reduction.

At present, the most common and easiest way to synthesise g-C_3N_4 is thermal polymerisation and the main precursors are cyanamide,[17,18] dicyandiamide,[19,20] melamine,[21–23] thiourea,[13,24] and urea.[25–27] The g-C_3N_4 synthesised from urea has a large specific surface area (146.35 $m^2\ g^{-1}$, determined by BET analysis), but its photocatalytic activity is not good enough due to the rapid electron–hole recombination.[28] Similarly, g-C_3N_4 materials synthesised from dicyandiamide and melamine have poor photocatalytic activity owing to their small specific surface area and fast electron–hole recombination rate.[28]

[a] *Materials and Chemistry (MatCh), Flemish Institute for Technological Research (VITO NV), Boeretang 200, Mol 2400, Belgium. E-mail: alessio.massaro@vito.be, vesna.middelkoop@vito.be*
[b] *Faculty of Bioscience Engineering, Ghent University, Coupure Links 653 Ghent, BE 9000, Belgium*
[c] *School of Engineering and Design, London South Bank University, London SE1 0AA, UK*
[d] *CNR-IPCF Bari Division, c/o Department of Chemistry of Università degli Studi di Bari, Via Orabona 4, 70126 Bari, Italy*

† Electronic supplementary information (ESI) available: Particle size distribution, photoluminescence emission, MB degradation, DART-MS. See DOI: https://doi.org/10.1039/d5qm00290g

However, literature reports indicate that the exfoliated g-C_3N_4 obtained from dicyandiamide and melamine shows the highest photocatalytic degradation performances.[28] To exfoliate this material, different methods have already been explored, including liquid exfoliation,[29,30] chemical blowing[31] and thermal etching.[32] Among these, thermal exfoliation has proven to be the most effective, synthesising g-C_3N_4 nanosheets with better electrochemical conductivity, smaller energy band gap, lower rate of recombination of photo-generated charges, less oxygen content and a more porous structure.[33]

In addition, the porosity of the material and the derived porous parameters, such as the specific surface area, pore volume, and pore size, also has a direct influence on the final catalytic properties.[34] Polymer or silica particles and their colloidal suspensions have been extensively used as templates to produce porous materials.[35–37] It was reported in the literature, that mesoporosity and macroporosity were successfully achieved in g-C_3N_4 by heating the mixture of cyanamide and colloidal silica nanosphere, followed by the removal of the silica template,[38] further widening the application and improving the characteristics of this material.

Given the promising aspects, this study aims to further study and test the C_3N_4 allotropic forms: g-C_3N_4 synthesised from melamine, and subsequently exfoliated using a thermal procedure, as well as the mesoporous graphitic carbon nitride (mpg-C_3N_4) synthesised starting from cyanamide.

Three-dimensional (3D) printing technologies have emerged as pivotal tools for the design and fabrication of complex geometries and devices that are easy to operate across multiple areas of application such as clean energy, environmental and sustainable chemistry.[39,40]

Specifically, digital light processing (DLP) 3D printing, a vat polymerisation technique, employs photochemistry to transform a photocurable resin into solid structures with exceptionally high resolution.[41] This approach offers significant advantages in the design of photocatalytic flow cells, as it enables the creation of highly customisable geometries that can optimise light pathways and fluid dynamics,[42] thus improving reaction kinetics in photocatalytic applications. Additionally, in comparison to traditional manufacturing methods, the precise control of the microstructure at the micrometer to millimeter scale,[41] possible through 3D printing, provides an excellent platform to design catalytic reactors with optimised porosity, surface area, and fluid channels.[43,44] Considering all these important aspects, in order to further enhance the efficiency of the C_3N_4-based photocatalytic materials, in this study we have integrated 3D printing, specifically DLP and direct ink writing (DIW), into the materials fabrication process. To the best of our knowledge, this work represents the first reported instance of cross-platform 3D printing (VAT photopolymerisation-based DLP and DIW) employing a C_3N_4-based ink, demonstrating also superior resolution in the shaping of catalytic bodies. There are only rare and very recent reports in the literature describing 3D printing of C_3N_4, namely DLP 3D printing of mpg-C_3N_4 by Luo *et al.* 2024 and DIW 3D printing of g-C_3N_4 by Liu *et al.*, 2024, employed as photocatalysts.[43,44] Liu *et al.* reported a 3D printed g-C_3N_4/geopolymer material with a high removal efficiency of methylene blue (MB) using only 3% g-C_3N_4 loading. Luo *et al.* replaced the extensive and challenging wash-coating procedures previously reported while printing a low C_3N_4 powder loading (1 wt%) of metal-free and nickel-containing mpg-C_3N_4 catalysts mixed with a resin, preserving the homogeneous dispersion of the C_3N_4-based catalysts in the resulting structured bodies.[44] In contrast, both the DLP and DIW methods presented in this work demonstrated facile 3D printing of structures with significantly higher catalyst concentrations of 5 wt% (for DLP) up to 88.5 wt% (for DIW), without employing the more complex engineered inline systems (blades and wipers) for mixing during the printing, broadening the scope of potential applications. Additionally, we explored the piezoelectric properties and electrochemical response of 3D printed g-C_3N_4 materials, with a particular focus on their ability to detect heavy metals through cyclic voltammetry, highlighting their potential for sensing applications. In fact, while some studies have examined the piezoelectric properties of g-C_3N_4, no research has thus far investigated these effects specifically in 3D printed g-C_3N_4 materials.

2. Experimental sections

Various C_3N_4 powders were synthesised by thermal polymerisation using melamine and cyanamide as precursors.

2.1. C_3N_4 synthesis

2.1.1. Synthesis of g-C_3N_4. g-C_3N_4 materials were synthesised by thermal polymerisation using melamine as precursor. The procedure was described as follows: 5.0 g of melamine (Aldrich, 99% purity) was placed into a 50 mL crucible with a cover, then the crucible was placed in a muffle furnace and heated up to 550 °C for 3 and 6 h with a heating rate of 5 °C min^{-1} in the air environment, then naturally cooled to room temperature. Additional commercially available g-C_3N_4 powder was obtained from C2CAT to serve as a reference material regardless of the exact parameters for its synthesis.

2.1.2. Exfoliation of g-C_3N_4. The nanosheets were prepared by thermal exfoliation of the bulk g-C_3N_4 obtained as above, following two distinct procedures. In the first method, g-C_3N_4 was exfoliated in static air as follows: 4.0 g of the bulk g-C_3N_4 was placed in an open ceramic container and was heated at 500 °C for 2 h with a ramp rate of 5 °C min^{-1}. A light-yellow powder of g-C_3N_4 nanosheets was finally obtained. In the second method, exfoliation occurred under a helium flow of 100 sccm. Here, 4.0 g of bulk g-C_3N_4 was placed in a ceramic crucible, covered with aluminium foil, and heated to 550 °C for 3 hours, with a heating rate of 10 °C min^{-1}. A light-yellow powder of g-C_3N_4 nanosheets was finally obtained.

2.1.3. Synthesis of mpg-C_3N_4. Mesoporous g-C_3N_4 was synthesised by thermally polymerising the cyanamide, using mono-dispersed colloidal silica as a hard template following a previous study.[38] Initially, cyanamide (6.0 g; Aldrich, 99% purity) was dissolved in Ludox AS-30 (20.0 g; Aldrich, colloidal silica with diameter of 12 nm, 30 wt% of SiO_2) in a 1 : 1 weight ratio of SiO_2 to cyanamide. The resulting mixture was slowly

evaporated at 60 °C while stirring it at low speed to form a white solid. The composite of cyanamide and silica was ground and put in a crucible with double lids and heated at 550 °C for 4 h in an ambient air condition to form the SiO_2/g-C_3N_4. The removal of silica nanoparticles from the synthesised mpg-C_3N_4 material is a critical step in ensuring the purity and structural integrity of the final product. To do so, the SiO_2/g-C_3N_4 composite was added into 4 M of NH_4HF_2 (17.1 g in 75.0 mL of solution; Aldrich, 95% purity) aqueous solution for 24 h under stirring, and the resulting yellow solid was separated by filtration and washed 4 times with 400 or 200 mL of water and 4 with 200 mL of ethanol. This purification process was repeated twice to ensure the complete removal of silica. The mesoporous g-C_3N_4 powder with the color of dark yellow was obtained by drying at room temperature for 24 hours.

2.2. 3D printing of C_3N_4

2.2.1. Digital light processing (DLP). To prepare the UV-curable printing slurry for vat photopolymerisation 3D printing, pre-treated C_3N_4 powders were mixed with commercially available UV-curable resins at a weight percent of 5% by first using mechanical mixing and then sonicating the slurry for 1 h, adding ice to the ultrasonic bath every 20 min to keep the dispersion temperature around 25 °C. One of the two UV-curable resins used was the "Standard Resin Neutral" (SRN), an acrylate-based resin, developed by Real, composed of hexamethylene diisocyanate and hexane-1,6-diol diacrylate as the main components, hexamethylene diacrylate as a diluent and diphenyl(2,4,6-trimethylbenzoyl)phosphine oxide as the photoinitiator. Additional prints were obtained using "Water Wash Resin +" (WWR), commercially available from Anycubic, previously reported by Luo *et al.* Improvements were made in the current work by prior milling and sieving of the powder to the required particle size distribution (PSD) resulting in an increased weight percentage of C_3N_4 in the ink. Additional information on the PSD and DLP printing parameters are provided in Fig. S1 and Table S1 (ESI†).

2.2.2. Direct ink writing (DIW). The three-dimensional micro-extrusion technique, also referred to as direct ink writing (DIW), was selected as shaping method for 3D printing of different C_3N_4 synthesised powders mixed with different polymers (methylcellulose, hydroxypropyl cellulose, silica and polysulfone).

g-C_3N_4/MC ink was prepared by mixing 6.17 g of a methylcellulose (MC) solution (3.5 wt%), 2.71 g of Ludox AS-40 and 10.50 g of g-C_3N_4 pretreated powder in a Thinky mixer, to ensure homogeneous dispersion.

g-C_3N_4/HPC ink was prepared by mixing 6.17 g of a hydroxypropyl cellulose (HPC) solution in 1-propanol (3 wt% 370 K, 4 wt% 100 K), 2.71 g of Ludox AS-40 and 10.50 g of g-C_3N_4 pretreated powder in a Thinky mixer, to ensure homogeneous dispersion.

g-C_3N_4/NP30 ink was prepared by mixing 25.64 g of Ludox CL-P, 7.01 g of g-C_3N_4 and 50.82 g of NP30 in a Thinky mixer.

Finally, the g-C_3N_4/PSF ink was prepared by mixing 5.05 g of a solution of polysulfone (PSF) in *N*-methyl-2-pyrrolidone (NMP) (35 wt%), 13.51 g of g-C_3N_4 and 1.64 g of NMP to adjust the rheology. The solidification of the resulting 3D print proceeded by immersion in a water-bath for approximately 12 hours to ensure the polymer precipitation and complete removal of NMP.

Further details on the DLP and DIW 3D printing can be found in Fig. S2 in the ESI.†

2.3. Characterisation

The crystal structures were characterised with X-ray diffraction (XRD), using a Malvern PANalytical Empyrean X-ray diffractometer with Co Kα radiation at 40 mA and 45 kV and a step size of 0.013 at a scan speed of 0.07° s^{-1}, over a 2θ range of 0–120°.

N_2 adsorption–desorption isotherms at 77 K for both g-C_3N_4 and mpg-C_3N_4 were measured using a Quantachrome Autosorb IQ gas sorption analyser. The morphology of the prepared samples was studied using a Keyence VHX 7000N digital microscope and by field emission scanning electron microscopy (FESEM, Nova NanoSEM 450, FEI). UV-vis absorption spectra in reflectance mode were collected at room temperature by means of a Cary 5000 (Varian) UV/Vis/NIR spectrophotometer equipped with an integration sphere to measure the diffuse reflectance. For the powders, 10.0 mg of the synthesised samples were dispersed in 2.0 mL of isopropanol, were left to stir 2 h, and were deposited in six layers on glass slides (1.5 × 1.5 cm^2), by drop-casting for each layer 50 μL of dispersion. Data acquisition was performed within the 300–800 nm wavelength range.

Steady-state PL emission spectra were acquired using a Fluorolog 3 spectrofluorometer (HORIBA Jobin-Yvon GmbH, Bensheim, Germany), equipped with double-grating excitation and emission monochromators and a 450 W Xe lamp as excitation light source. PL emission spectra were recorded using excitation wavelengths at 300, 320, 350, 375, 400, 420, 450 and 485 nm for all samples. Time-resolved PL (TRPL) measurements were carried out by Time Correlated Single Photon Counting (TCSPC) technique, with a FluoroHub (HORIBA Jobin-Yvon). CDs solutions were excited using 80 picosecond laser diode sources at 375 nm (NanoLED 375L), with a time resolution of ~300 ps for all the measurements. Data collection was conducted over a time window of 0 to 100 ns.

The Fourier transform infrared (FTIR) spectra were recorded on a Nicolet iS10 FTIR spectrometer in the range of 500–4000 cm^{-1} for detecting the bonding vibrations.

The 3D printed samples exposed to model organic solvents were characterised using direct analysis in real time mass spectrometry (DART-MS), using a thermo Q exactive orbitrap mass spectrometer in positive and negative ionisation modes, in the *m*/*z* range of 0–1300. Rheologic measurements of the DLP resins and DIW inks were performed using a Haake Mars 60 Rheometer at 25 °C, using a plate-plate configuration with a cone–plate and a gap of 1 mm.

In addition, the surface topographies and piezoelectric responses of the C_3N_4 powders and DIW 3D-printed samples cured in air at 550 °C were characterised using Piezoresponse Force Microscopy (PFM). Measurements were performed with a conductive SCM-PIT-V2 Atomic Force Microscopy (AFM) probe (Bruker), applying 10 V bias to the tip at a frequency of 50 kHz. The C_3N_4 powder sample was prepared by suspending in EtOH

with concentration of 50 ppm followed by ultrasonication for 30 min. A 50.0 μL aliquot of the suspension was drop-cast onto a non-conductive flat support (MICA muscovite, Sigma-Aldrich) and dried under a flow of air. The 3D printed C_3N_4 structure was characterised in its original form.

2.4. Photocatalytic activity tests

The photocatalytic activities of the synthesised samples were evaluated by monitoring the degradation of a 0.02 mM methylene blue (MB) solution under controlled conditions. The experiments were carried out using a solar simulator (LSH-7320, MKS Newport) with an intensity of 1 sun (1 kW m^{-2}). In each experimental run, 100.0 mg of the synthesised photocatalyst was dispersed in 150.0 mL of the 0.02 mM MB solution. The mixture was continuously stirred using a magnetic stirrer set to a speed of 250 rpm to ensure uniform dispersion of the catalyst and proper interaction between the photocatalyst and the dye molecules. At regular intervals of 30 minutes, 2.0 mL of the reaction mixture were extracted for analysis. The concentration of residual MB in the solution was determined by measuring its absorbance using a Shimadzu UV-1800 spectrophotometer. The absorbance values were recorded at the characteristic maximum absorption wavelength of MB (~664 nm). The remaining concentration of MB in the solution at each time point was calculated using a calibration curve equation.[45]

2.5. Electrochemical measurements

To demonstrate the detection capability of the 3D printed DLP samples for Pb^{2+}, cyclic voltammetry (CV) measurements were conducted using a three-electrode setup. A glassy carbon electrode (GCE) was employed as the working electrode, with an Ag/AgCl reference electrode and a graphite rod counter electrode. The potential was scanned from −1 to 0 V with a scan rate of 100 mV s^{-1}. Prior to modification, the bare GCE was meticulously polished with felt pads using an alumina slurry to achieve a mirror-like surface. The electrode was then rinsed with deionised water and sonicated for a specific duration to minimise adsorbed contaminants. Finally, the treated electrode was dried before further use. For the first experiment, a dispersion of 5.0 mg of bulk g-C_3N_4 in 4.0 mL of Nafion (0.25 wt%, in ethanol) was prepared and sonicated for 30 minutes. In the subsequent two experiments, the same bulk g-C_3N_4 based DLP mixtures used for the 3D printing were employed. The prepared dispersions were drop-cast onto the GCE surface using a micropipette and left to dry or cure at room temperature before performing CV measurements. Each sample was tested under two conditions: (a) immersion in a 0.1 M acetic acid–sodium acetate (HAc–NaAc) buffer solution (pH = 5) and (b) in a $Pb(NO_3)_2$ solution (400 μM) in the same buffer.

3. Results and discussion

3.1. Characterisation

g-C_3N_4 and mpg-C_3N_4 samples were synthesised *via* thermal polymerisation. Specifically, for mpg-C_3N_4, cyanamide was polymerised in the presence of silica nanoparticles, used as hard templates, at 550 °C.

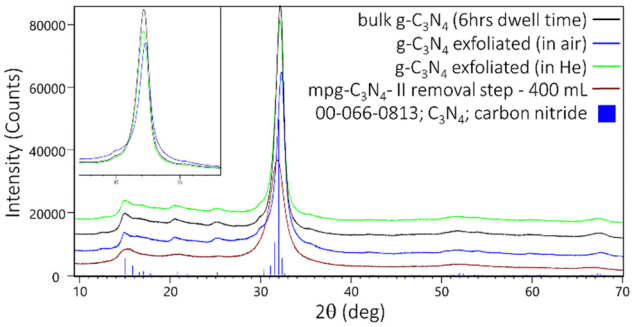

Fig. 1 XRD patterns of all the g-C_3N_4 powders prepared in this study. Expected peak positions for the C_3N_4 compound are also indicated.

The XRD patterns of the synthesised powders (g-C_3N_4 synthesised using 6 h dwell time, g-C_3N_4 exfoliated in static air, g-C_3N_4 exfoliated under helium, and mpg-C_3N_4) are presented in Fig. 1, illustrating a comparative analysis of their crystalline structures. All samples show similar XRD patterns. Specifically, the sharp strong peak observed at 2θ = 32.2° corresponded to the (002) facet of g-C_3N_4 attributed the stacking of conjugated aromatic layers.[46]

Furthermore, after the exfoliation of the g-C_3N_4, a broadening of the (002) peak can be observed. In the exfoliating process, since some inter-layer hydrogen bonds were destroyed and the number of layers was reduced,[47] the peak of the exfoliated powder results broader compared to that of pristine g-C_3N_4. The reflection peak for the non-exfoliated powder at 32.2° is shifted to 32.3° after the exfoliation in air, corresponding to a decrease of the lattice plane distance.[48]

SEM analysis (Fig. 2) confirms the successful exfoliation of g-C_3N_4. Specifically, in the case of bulk g-C_3N_4, flat, aggregated and non-porous flakes were observed. As shown in the image, the samples treated with the two different thermal exfoliation procedures are composed of thinner layers with rough surface and layered detachments (Fig. 2B and C). There were similar reports in the literature for the exfoliated g-C_3N_4.[48–50]

Moreover, in comparing the g-C_3N_4 exfoliated under static air (Fig. 2B) with that exfoliated in He (Fig. 2C), distinct differences in the exfoliation degree become apparent. The powder exfoliated under static air exhibits a relatively low degree of exfoliation, whereas the powder exfoliated in He displays a significantly higher level of layers formation, which translates in an increase of the photocatalytic surface area.

The basis of the thermal exfoliation lay in the hydrogen-bond cohered strands of polymeric Melon units in the layers (particularly for short ones), which are not stable enough against (or reactive to) oxidation process in air and so will be gradually oxidized away from the bulk material so that the thickness of bulk g-C_3N_4 will be decreased to the desired nanoscale.[51]

Additionally, Fig. 2 highlights the distinction between the bulk g-C_3N_4 and the mpg-C_3N_4: indeed, the mpg-C_3N_4 exhibits a three-dimensional sponge-like framework with an

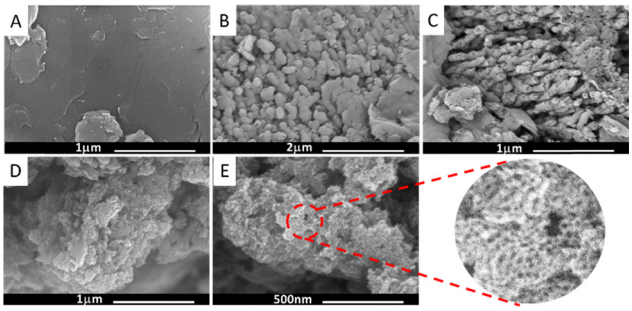

Fig. 2 SEM images of (A) non-exfoliated g-C_3N_4. Scale bar: 1 μm; (B) exfoliated g-C_3N_4 (in air). Scale bar: 2 μm; (C) exfoliated g-C_3N_4 (in He). Scale bar: 1 μm; (D) mpg-C_3N_4. Scale bar: 1 μm; (E) SEM image showing the mesoporous structure of the synthesised mpg-C_3N_4. The magnified view highlights the porosity originated by the SiO_2 NP. Scale bar: 500 nm.

interconnected porous structure. This structure is formed through two processes: the silica nanoparticle template creates small pores of approximately 12 nm in diameter (Fig. 2), while the gas released during cyanamide decomposition generates larger pores. This combined porosity could enhance the light scattering under irradiation and provide more interfacial contact between the aqueous solution and the solid catalyst. The specific surface area measurements of the C_3N_4 powers are presented in Table 1.

Fig. 3 presents the FTIR spectra of the g-C_3N_4 and mpg-C_3N_4 samples. Broad peaks between 3000 and 3500 cm^{-1} can be attributed to N–H stretching vibration modes. This result indicates that uncondensed amino functional groups still exist in the products. The several bands in the 1200–1650 cm^{-1} region correspond to the typical stretching modes of C–N heterocycles,[52] confirming the successful formation of g-C_3N_4. Finally, the sharp absorption peak at approximately 805 cm^{-1} is due to the typical breathing mode of tri-*s*-triazine units.[52]

The absorption spectrum of the exfoliated g-C_3N_4 in He (Fig. 4A) showed a significant red shift (390 to 398 nm) in comparison with the bulk g-C_3N_4. This may be attributed to the high temperature intrinsic modification of the porous structures, formed during the thermal exfoliation process. This observation is in agreement with other trends reported for g-C_3N_4 exfoliated with thermal treatments of bulk g-C_3N_4.[33] Both powders, as well as the reference powder, display an absorption edge around 460 nm, corresponding to a bandgap of 2.70 eV (calculated with the Tauc plot method).

Table 1 Specific surface areas of g-C_3N_4, reference g-C_3N_4, exfoliated g-C_3N_4 (He) and mpg-C_3N_4, calculated from N_2 adsorption isotherms using the BET and BJH methods

Powder	Surface area (BET) (m^2 g^{-1})	Surface area (BJH) (m^2 g^{-1})
Bulk g-C_3N_4	7.3	6.4
Reference bulk g-C_3N_4	7.5	6.2
Exfoliated g-C_3N_4 (air)	7.4	Not calculated
Exfoliated g-C_3N_4 (He)	11.5	9.4
mpg-C_3N_4	125.1	117.0

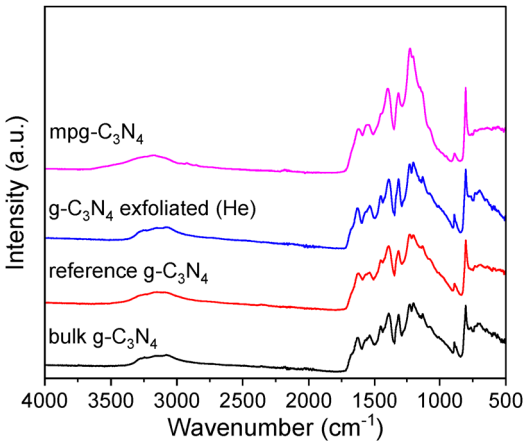

Fig. 3 FTIR spectra in absorbance mode of not exfoliated g-C_3N_4, the reference g-C_3N_4 powder, exfoliated g-C_3N_4 (in He) and mpg-C_3N_4.

Furthermore, the absorption spectrum (Fig. 4A) of mpg-C_3N_4 shows a wide absorption band at wavelengths greater than 400 nm, in accordance with data reported in the literature.[44] Similar absorption features were also observed in the spectra of

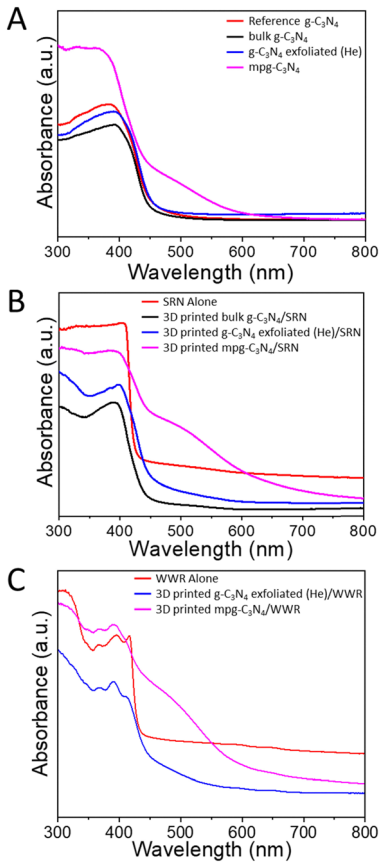

Fig. 4 (A) UV-vis absorption spectra of all the synthesed powders: bulk g-C_3N_4, exfoliated g-C_3N_4 (He), mpg-C_3N_4 compared to the reference g-C_3N_4 powder. (B) UV-vis absorption spectra of DLP 3D printing photosensitive inks: bulk g-C_3N_4 and the reference g-C_3N_4 powder, exfoliated g-C_3N_4 (in air), mpg-C_3N_4 dispersed in the SRN resin compared to (C) the SRN resin.

the DLP 3D printed mpg-C_3N_4 samples. In addition, compared to the one of bulk g-C_3N_4, the spectrum also shows a slight blue shift due to the quantum confinement effect, where light absorption of mpg-C_3N_4 is slightly shifted to high energy region.[50,53]

Characterisation measurements related to the 3D printed resins, are reported in Fig. S4–S6 (ESI†).

Fig. 5 provides a comparison of the steady state photoluminescence spectra of the non-exfoliated, exfoliated and mpg-C_3N_4 in powder and after incorporation in the DLP resin. All samples show an intense luminescence in the blue-green region of the spectrum, which is independent of the excitation wavelength for all samples (Fig. S5 and S6, ESI†), with only a slight broadening at longer wavelengths for the He exfoliated samples (Fig. S5C and D, ESI†). Instead, a significant difference is observed for the mpg-C_3N_4 powders, with the clear identification of a double emission band extending into the red. In agreement with what has been reported in the literature, since the band gap states have been attributed to the sp^3 C–N σ band,[32] the sp^2 C–N π band and the lone pair (LP) state of the bridge nitride atom, the radiative emission can derive from π*–π, σ*–LP or π*–LP transitions.[54] The incorporation of g-C_3N_4 into the resin does not produce significant differences in the emission spectra, which are comparable and superimposable (Fig. 5A and C), indicating that the photoemissive properties of the powders are not influenced, in the spectral shape, by the polymer matrix. A moderate quenching of the emission in the green is observable only for the mpg-C_3N_4 powders incorporated into the resin. The time resolved profiles, for mpg-C_3N_4 and for g-C_3N_4 exfoliated in He and incorporated in resin, presented in Fig. 5D–F, overlap, indicating a static quenching since the resin does not modify the recombination dynamics. In contrast, a clear difference is observable for the sample in Fig. 5B, which has a slower lifetime when incorporated into the resin matrix, showing a passivating effect on the luminescence. Compared to the DLP 3D printed mpg-C_3N_4/SRN sample, its mpg-C_3N_4/WWR analogue exhibits a more pronounced intensity of the emission spectrum in the green wavelength region (Fig. 5I).

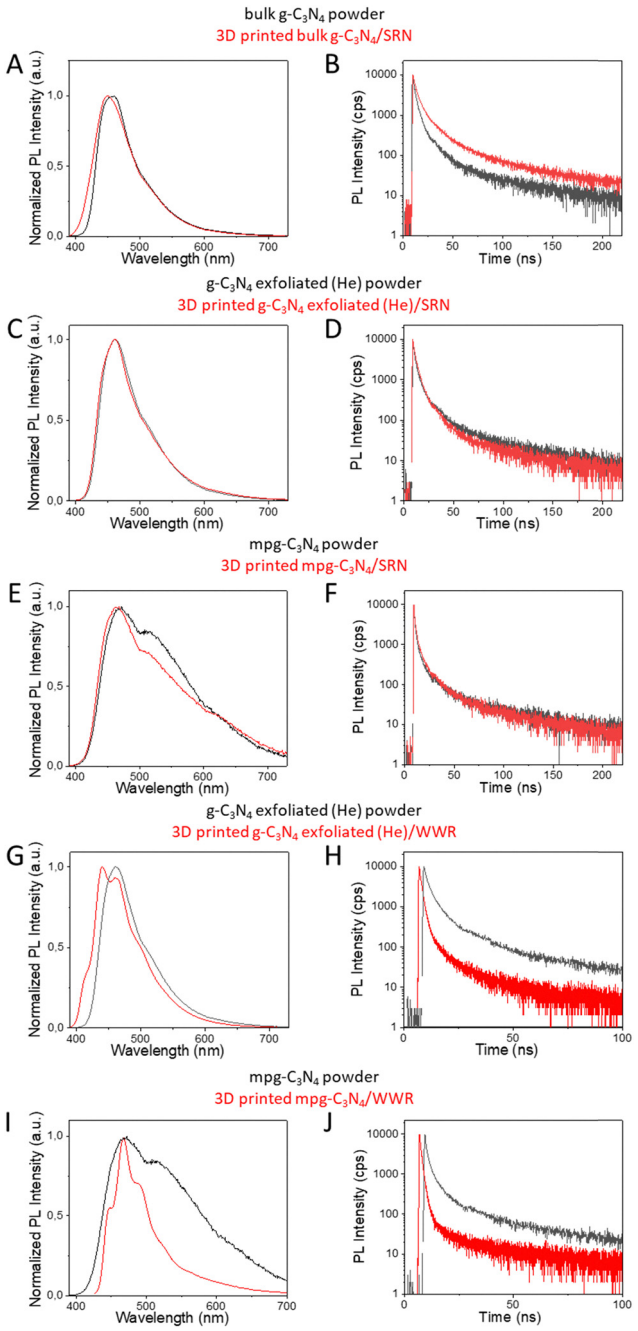

Fig. 5 Photoluminescence emission spectra and time-resolved spectroscopy of DLP 3D printed C_3N_4 of the three powder forms dispersed in the DLP SRN and WWR resins: bulk (A and B), exfoliated (in He) (C, D, G and H), and mpg-C_3N_4 (E, F, I and J), compared to their starting powders.

Time-resolved photoluminescence measurements further reveal a notably faster decay trend of the excited-state species when the photocatalyst is incorporated into the WWR resin, in contrast to its pristine powder form. This effect is likely attributable to a higher density of non-radiative relaxation pathways or modifications in the local environment.[55] These findings suggest that the distinct chemical nature of the WWR resin matrix has a greater impact on the excited-state dynamics compared to the that of the SRN resin.

Digital microscope images (Fig. 6) of the 3D printed samples reveal that the final particle dimensions within the DLP structures were consistently below 10 μm for all powders. This aspect contributed significantly to achieving a high precision in the printing of the geometries. Notably, when the powder forms big micron-sized aggregates, it induces significant light scattering during the photocuring process, which in turn reduces the printing resolution. Similarly, the DIW ink demonstrated excellent printability, exhibiting no clogging or interruptions during the extrusion process.

3.2. Stability tests in model solvents

Following optimisation of the printed samples, their stability tests were conducted in organic solvents (water, acetonitrile, hexane, methanol) typically used in various synthesis of Active Pharmaceutical Ingredients (APIs). To do so, each sample has been placed in a Petri dish and covered with approximately

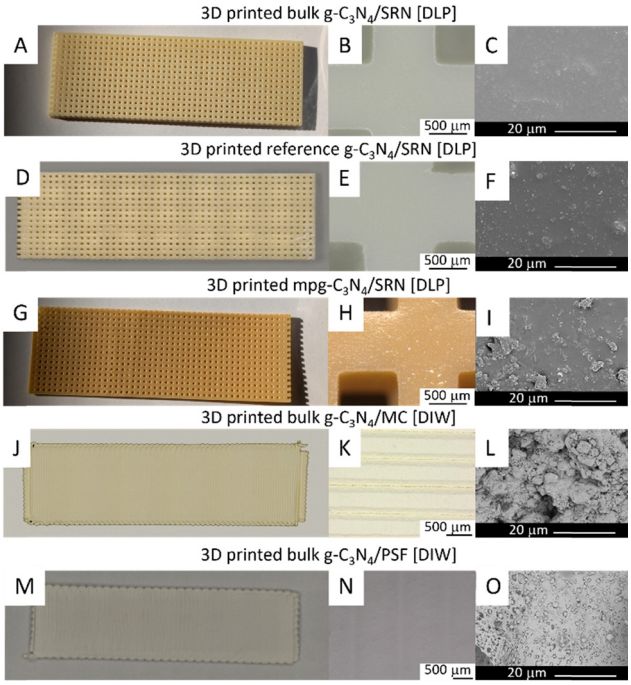

Fig. 6 Digital images (A, D, G, J and M), digital microscope images (B, E, H, K and N; scale bars: 500 µm) and SEM images (C, F, I, L and O; scale bars: 20 µm) of different 3D printed samples with the different powders.

40.0 mL of the organic solvent and left for a fixed number of hours under stirring. All the samples, including the DIW sample, demonstrated extraordinary stability in acetonitrile, without showing swelling or any mass changes within the measurement sensitivity of ±0.1 mg after 24 h. However, only the DLP 3D printed samples obtained using the WWR resin displayed limited stability in acetonitrile, as evidenced by the structural degradation observed after 24 hours of immersion. Following this, the DIW 3D printed bulk g-C_3N_4/WWR sample was analysed using the DART-MS, which revealed that after immersion in acetonitrile, the DLP 3D printed structure exhibited a reduced concentration of the photoinitiator (see Fig. S18 and S19, ESI†).

The cause of the instability of the WWR-based samples is its chemical composition. Specifically, the SRN resin consists primarily of organic compounds, such as hexamethylene diisocyanate, hexamethylene diacrylate and hexane-1,6-diol. These molecules feature polar functional groups at the endings and a relatively long nonpolar aliphatic backbone, contributing to an overall hydrophobic character. In contrast, the WWR resin is based on organic compounds like polyethylene glycol diacrylate, which contains a repeating ethylene oxide (–CH_2CH_2O–) backbone. The presence of ether linkages increases the polarity and hydrophilicity of the resulting polymeric matrix.

Additionally, also the DIW 3D printed bulk g-C_3N_4/PSF sample was analysed using the DART-MS (Fig. S18, ESI†), which confirmed that the composition of the 3D printed structure remained unchanged after immersion in acetonitrile. All the resulting samples were stable, also in hexane and methanol, without showing swelling or deformation. In these two last solvents, the DLP structures showed, respectively, a mass change of just 0.18% and 0.95% after 72 h of exposure to the solvents. Similarly, all samples exhibited strong stability in water, with the exception of the DIW samples printed with MC and HPC, which displayed swelling and deformation due to the chemical nature of the binder.

3.3. Testing for the degradation of MB

3.3.1. Photodegradation of MB. As shown in Fig. 7, the performance of the synthesised C_3N_4 samples in the degradation of MB using solar light, and the dye removal percentages were calculated using eqn (1).

$$\%\text{Removal} = \frac{C_0 - C_t}{C_0} \times 100 \quad (1)$$

where: C_0: is the original concentration of MB (mM); C_t: is the concentration of MB (mM) remained in the solution by the time of the measurement; k: is the rate of degradation reaction.

The photocatalytic performances of the C_3N_4 samples were categorised into three groups based on their MB removal efficiency after 180 minutes of irradiation: low, average, and high performance. The low-performance group includes 3D printed bulk g-C_3N_4/MC and 3D printed mpg-C_3N_4/SRN, both of which exhibited less than 40% MB removal, indicating limited photocatalytic activity. The average-performance category consists of four samples: 3D-printed mpg-C_3N_4/WWR with 55% MB removal, bulk g-C_3N_4 powder with 63%, 3D printed g-C_3N_4 exfoliated (He)/WWR with 69% MB removal and 3D printed bulk g-C_3N_4/PSF with 77% MB removal. Among all the synthesised samples, the mpg-C_3N_4 powder demonstrated the highest photocatalytic efficiency, likely due to its larger surface area (Table 1), achieving an impressive 92% MB removal after 180 minutes of irradiation. These findings highlight the effect of various processing routes to the photocatalytic performance of the C_3N_4 samples.

Furthermore, the rates of these photo-degradation reactions (k) are analysed using eqn (2), the visualisation of these

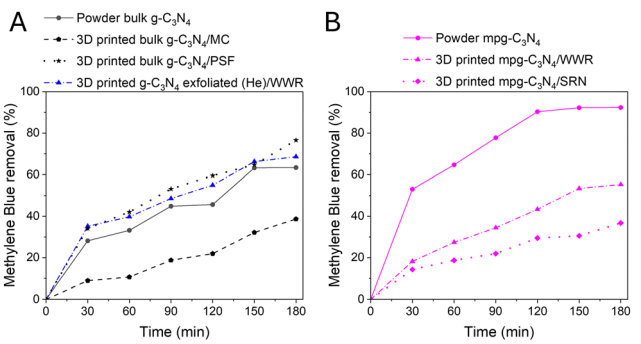

Fig. 7 MB removal (photocatalytic degradation + adsorption) using the 3D printed g-C_3N_4 formulations (panel A), mpg-C_3N_4 formulations (panel B) compared to the starting powders under solar simulator with the intensity of 1 kW m^{-2}.

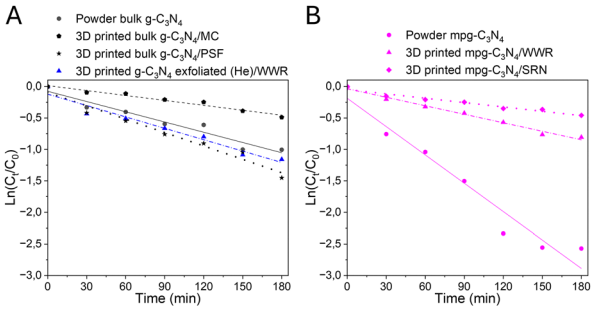

Fig. 8 The rate constant of photo-degradation reaction using the 3D printed g-C_3N_4 formulations (panel A) and 3D printed mpg-C_3N_4 formulations (panel B) compared to the starting powders.

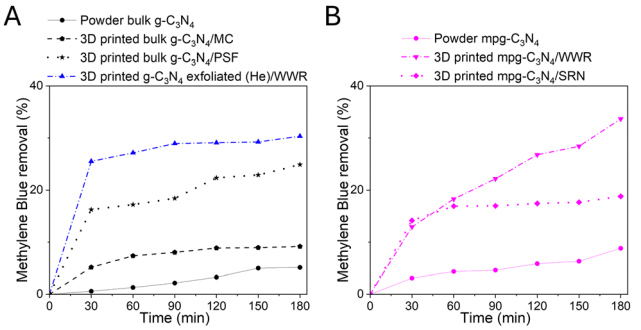

Fig. 9 The dye adsorption capacity q_t (mg g^{-1}) of the 3D printed g-C_3N_4 formulations (panel A) and 3D printed mpg-C_3N_4 (panel B) formulations compared to the starting powders.

equations are depicted in Fig. 8.

$$\ln\left(\frac{C_t}{C_0}\right) = -kt \quad (2)$$

The rate constant (k) is determined by the slope of the fitted trendline, and the rate constant for each sample is computed and summarised in Table 2.

The adsorption capacity of a catalyst plays a crucial role in determining its overall performance. To assess the adsorption capabilities of the synthesised samples, experiments were conducted under the same conditions as the photocatalytic tests, with the key difference being the absence of a light source to determine the effect of adsorption from photocatalysis. The adsorption capacity of each sample was systematically measured using eqn (3).[56]

$$q_t = \frac{(C_0 - C_t) \times V \times M_{\text{methylene blue}}}{m} \quad (3)$$

where: q_t (mg g^{-1}): the adsorption capacity of the synthesised sample at the certain time t; $M_{\text{Methylene blue}}$ (g mol^{-1}): the molecular weight of the dye methylene blue; m: the amount of catalyst used.

As illustrated in Fig. 9, the 3D printed mpg-C_3N_4/WWR sample exhibited the highest adsorption capacity, achieving 34% MB removal solely through adsorption after 180 minutes in the dark. This was followed by the 3D printed g-C_3N_4 exfoliated (He)/WWR sample, which demonstrated a slightly lower but still high MB removal efficiency of 30%. Interestingly, both samples fall within the average photocatalytic performance category, suggesting that their improved overall dye removal efficiency is primarily driven by their adsorption capacity rather than their photocatalytic activity. In contrast, the mpg-C_3N_4 powder, which demonstrated the highest photocatalytic performance with 92% MB degradation, exhibited a notably low adsorption capability, with only 9% MB removal attributable to adsorption. This result confirms that, in this case, the primary mechanism driving MB degradation is photocatalytic activity rather than adsorption.

Table 2 The summary of estimated rate constant of dye degradation reaction using the synthesised C_3N_4 as photocatalyst

Samples	Rate constant × 10^{-3} (min^{-1})	Coefficient R^2 (%)
Powder bulk g-C_3N_4	5.4	95
Powder mpg-C_3N_4	15.0	95
3D printed g-C_3N_4 exfoliated (He)/WWR	6.0	96
3D printed mpg-C_3N_4/WWR	4.5	99
3D printed mpg-C_3N_4/SRN	2.3	96
3D printed bulk g-C_3N_4/MC	2.6	97
3D printed bulk g-C_3N_4/PSF	7.1	97

The kinetic model of the adsorption process was investigated using pseudo first and second order.[57] The calculated data and trendlines are illustrated in Fig. S12 (ESI†).

The rate constant of the synthesised samples following each kind of kinetic model are summarise in Table S1 (ESI†). By comparing the coefficient R^2 value, the fitted kinetic model for the adsorption process of each sample was determined. The samples followed first order kinetic includes bulk g-C_3N_4 in powder form and the DIW 3D printed bulk g-C_3N_4/MC, and the rest 5 samples fitted the second order kinetic better.

The 3D printed samples developed in this study demonstrate a significantly improved photocatalytic performance compared to the 3D printed g-C_3N_4/geopolymer composite reported by Liu *et al.*, 2024.[43] Their material exhibited an MB removal efficiency of 94% within 60 minutes under dark conditions; however, 82% of this is due to adsorption, meaning only 12% of MB was effectively degraded, while the remaining fraction was mainly adsorbed, requiring a regeneration of the material before being used again. Additionally, as highlighted in their study, increasing the g-C_3N_4 content beyond 3 wt% negatively impacted the adsorption capacity, thereby limiting the overall removal efficiency. In contrast, the best-performing 3D printed sample presented in this work (DIW 3D printed bulk g-C_3N_4/PSF) achieved a photodegradation efficiency of 42% within 60 minutes, with adsorption contributing only 17%. Notably, after 180 minutes, the total MB removal reached 77%, demonstrating a higher degree of degradation rather than mere adsorption. Tables 3 and 4 compare the photocatalytic performance of the best 3D printed formulation presented in this study (DIW 3D printed bulk g-C_3N_4/PSF) with representative g-C_3N_4-based, and typical photocatalysts reported in the literature, respectively,

Table 3 Comparison of MB degradation efficiency for DIW 3D printed g-C_3N_4/PSF in this work with different g-C_3N_4-based photocatalysts in 3D printed and monolithic forms as reported in the literature

Material	Fabrication method	Catalyst loading (%)	Contact time	Removal efficiency	Adsorption (%)
g-C_3N_4/PSF	DIW	88	180 min	77	22%
g-C_3N_4 filter[58]	Monolith	100	9 filtrations	60	60%
g-C_3N_4 geopolymer[43]	DIW	3	60 min	94	82%
g-C_3N_4 sponge[59]	Monolith	100	60 min	~55	Theoretically 0%
Au/CN–SA aerogel[60]	DIW	96	Overnight (dark) + 60 min	93	~67%
g-C_3N_4/Fe_3O_4[61]	Pellet	100	60 min (dark) + 100 min	89	Not specified

which achieved MB degradation levels ranging from 46.6% to 94% within 60–180 min.

3.3.2. Piezoelectric degradation of MB. In this study, the piezoelectric activity was evaluated using sonication energy. The experiments utilised the same amounts of synthesised C_3N_4 samples and MB solutions as in the photocatalysis tests. However, instead of exposing the mixture to a solar simulator, it was placed in a sonication bath. The remaining MB concentration in the mixture was measured every 30 minutes.

As depicted in Fig. 10, the results of the piezoelectric degradation of MB demonstrated that the synthesised mpg-C_3N_4 and bulk g-C_3N_4 powders exhibited significantly high piezoelectric activity. Under sonication alone, these samples successfully reduced the MB concentration by 85% and 81%, respectively, indicating their strong piezoelectric response in facilitating dye degradation. When considering both adsorption effects and the contribution of sonication alone, it becomes evident that the remaining five synthesised samples exhibited relatively low piezoelectric activity. These could be attributed to variations in their structural properties, such as crystallinity, porosity, and intrinsic piezoelectric characteristics, which directly influence their ability to generate charge carriers when mechanical force applied. To further understand the degradation efficiency, the reaction kinetics were analysed and are visually represented in Fig. 11, illustrating the degradation trends over time. Additionally, the calculated rate constants for each sample are summarised in Table S2 (ESI†), providing a quantitative comparison of their piezoelectric degradation efficiencies. Alternatively, Fig. 7–11 with split panels A and B are available as Fig. S15–S21 (ESI†) in each of which profiles for all 3D printed C_3N_4 formulations and starting powders are overlaid together for direct comparison. A comparison of the degradation efficiency of MB for the mpg-C_3N_4 powder synthesised in this work with different piezocatalyst powders reported in the literature is presented in Table 5.

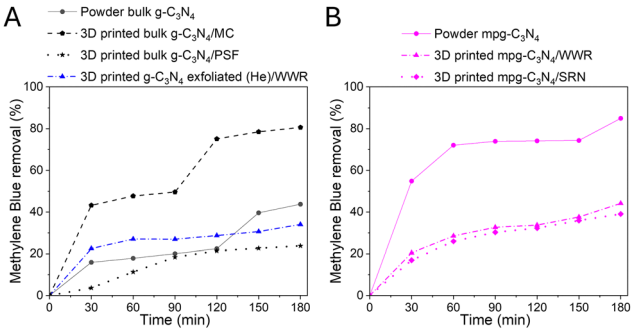

Fig. 10 Piezocatalytic degradation: dye removal efficiencies (%) of 3D printed g-C_3N_4 (A) and mpg-C_3N_4 (B) formulations, as well as their respective starting powders, under ultrasonic excitation in the dark.

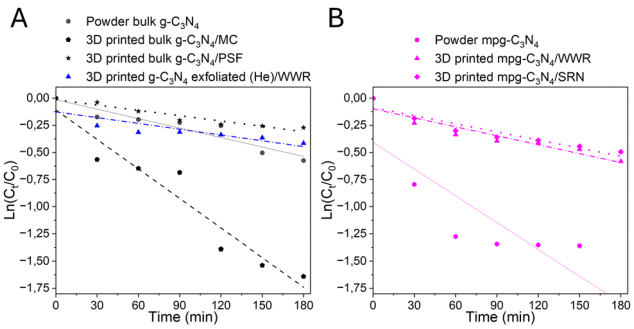

Fig. 11 Rate constants for dye removal *via* piezocatalysis using 3D printed g-C_3N_4 (A) and mpg-C_3N_4 (B) samples, compared to their respective starting powders.

Table 4 Comparison of MB degradation efficiency (%) for DIW 3D printed g-C_3N_4/PSF from this work with different photocatalysts in 3D printed and monolithic forms reported in the literature

Material	Fabrication method	Contact time	Removal efficiency (%)
g-C_3N_4/PSF	DIW	180 min	77
TiO_2/chitin/cellulose[62]	DIW	60 min (dark) + 180 min	80
TiO_2/Al_2O_3[63]	Binder jetting	240 min	47
TiO_2/ZnO[64]	SLA	30 min + 180 min	~62
FeCp/Fe_3O_4[65]	Powder	120 min	78

3.4. Testing of the piezoelectric effect

g-C_3N_4 has recently been found to exhibit strong piezoelectric responses, attributed to its non-centrosymmetric structure and large specific surface area.[15] However, to the best of our knowledge, there is no research on the piezoelectric properties of 3D printed g-C_3N_4 structures.

To evaluate the piezoelectric properties of the bulk g-C_3N_4 powder and DIW 3D-printed bulk g-C_3N_4/MC structures, PFM measurements were performed. The PFM results are presented in Fig. 12 and 13. Specifically, the bulk g-C_3N_4 powder appears as agglomerates composed of particles ranging in sizes from

Table 5 Comparison of MB degradation efficiency (%) of mpg-C_3N_4 powder synthesised in this work with various piezocatalyst powders reported in the literature

Material	Contact time (min)	Removal efficiency (%)
mpg-C_3N_4	180	85
$BaBi_4Ti_4O_{15}$[66]	120	40
$BaTiO_3$[67]	60	77
$Bi_2VO_{5.5}$[68]	180	32
ZnO/CuO[69]	140	71

~150 nm to 1–2 μm (Fig. 12A and B), which is in agreement with particle size distribution measurements. For this sample, both vertical and lateral piezoresponses were detected (Fig. 12C–F). The phase plot in Fig. 12D shows that the bulk g-C_3N_4 powder sample exhibits a vertical piezo phase ranging from −20.1° to 99.4°. Although this range indicates the presence of a piezoelectric response, as confirmed by the amplitude plot (Fig. 12C), the phase shift remains significantly lower than the 180°. This could be due to random orientation of g-C_3N_4 molecular sheets in the agglomerate, which leads to compensation piezo-effect vectors directed antiparallel. Lateral piezo effect amplitude is lower than the vertical one. These results are consistent with those reported in the literature.[16] However, after the 3D printing and subsequent calcination procedures, the vertical piezo phase signal change expanded reaching values from −179.2° to 168.3° (Fig. 13D). This substantial increase, along with the overall piezo amplitude increase by almost one order of magnitude (Fig. 13C) confirm an enhanced piezoelectric response. Such increase can be induced by structural rearrangements and improved piezo domain alignment during the calcination process as well as increasing crystallinity of the material.

Ultimately, this approach enabled the fabrication of a DIW 3D printed g-C_3N_4-based sample with a notable piezoelectric response.

3.5. Electrochemical measurements

In recent years, g-C_3N_4 has been studied in the literature for its application in electrochemical sensors, particularly for the detection of heavy metals.[70,71] However, to the best of our knowledge, this is the first study to investigate the detection capabilities of g-C_3N_4-based structures obtained *via* DLP 3D printing. The results of the CV characterisations of detection of

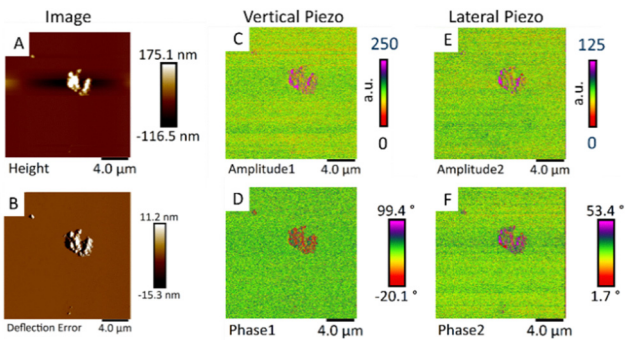

Fig. 12 PFM analysis of g-C_3N_4 powder. AFM topography image (A), deflection error image (B). Vertical piezoresponse amplitude (C) and phase images (D). Lateral piezoresponse amplitude (E) and phase images (F).

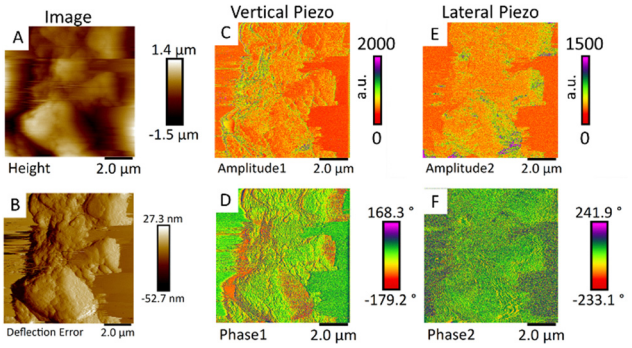

Fig. 13 PFM analysis of DIW 3D printed bulk g-C_3N_4/MC structure, heat-treated at 450 °C. AFM topography (A) and deflection error images (B). Vertical piezoresponse amplitude (C) and phase images (D). Lateral piezoresponse amplitude (E) and phase images (F).

metal content in a representative $Pb(NO_3)_2$ model solution are reported below. As shown in Fig. 14, for both DLP resins a distinct peak was observed at approximately −0.5 V, indicating a clear electrochemical response. Specifically, the DLP 3D printed bulk g-C_3N_4/SRN sample exhibited a higher electrochemical response to model heavy metal Pb^{2+} ions. The responses of the two resins can be directly compared to that of g-C_3N_4 with Nafion which is commonly reported in the literature.[70] The lower sensitivity observed in the electrodes prepared with DLP resin compared to those with Nafion is not only due to the different chemical structure and properties of the binders contained in the DLP resins but can be attributed to differences in binder concentration. While the amount of powder used in all experiments was kept constant, the binder content varied significantly. In the case of Nafion, the polymer concentration in the solution used for drop-casting was notably low (0.25 wt%). Conversely, for the DLP resin, the exact binder content remains unknown, as the detailed formulation is not disclosed. However, based on available commercial information, the solvent content in both resins could be estimated to be in the range of 40–60 wt%. This suggests that the polymer concentration in the drop-casting solution was substantially higher than in Nafion, leading to a different powder/polymer ratio which influenced the intensity of the observed signal. Taking this in consideration, the results obtained using both DLP resins demonstrated that the printed electrodes exhibit sensitivity to Pb^{2+}. This suggests that further optimisation of the material formulation and processing conditions could enhance their performance, making them viable candidates for sensor applications in heavy metal detection.

4. Conclusion

In this study, DLP and DIW 3D printing techniques were successfully employed for the direct fabrication of stable and active C_3N_4-based structures. Notably, this work presents the first instance of direct printing of C_3N_4 materials without the necessity of coating previously printed structures. This eliminates the need for high-temperature post-printing treatment processes typically required in other 3D printing methods that

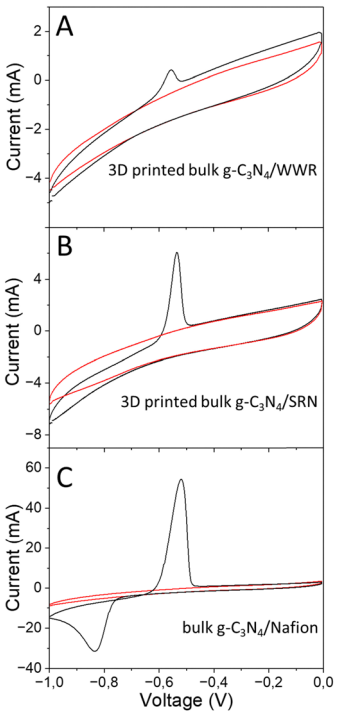

Fig. 14 Cyclic voltammograms of DLP 3D printed bulk g-C_3N_4 with SRN resin (A), WWR (B) and bulk g-C_3N_4/Nafion dispersion (C) toward Pb^{2+} detection on bulk g-C_3N_4-modified GCE in an electrolyte solution of 0.1 M HAc–NaAc (pH = 5). The red line represents the cyclic voltammogram of the sample in the buffer solution alone, while the black line corresponds to the cyclic voltammogram of the sample in the same buffer solution with the addition of $Pb(NO_3)_2$, resulting in a 400 μM concentration of Pb^{2+}.

frequently lead to alteration or degradation of the C_3N_4 properties. Both the developed DLP and DIW formulations were printable into desired geometries with a high resolution.

The current work highlights the need for tailored formulations of the printable inks with appropriate polymer binders and 3D printing parameters to preserve their specific photo, piezo and electro-catalytic performance.

The photocatalytic MB degradation efficiency has been tested for all representative 3D printed formulations. The highest removal efficiencies were observed for DIW 3D printed g-C_3N_4/PSF formulation (71%), followed by DLP 3D printed g-C_3N_4-WWR based formulations (63%). All formulations showed a similar level of piezoelectric degradation (41%) with only DIW 3D printed bulk g-C_3N_4/MC exceeding that level (81%). In addition, PFM analysis of both powdered bulk g-C_3N_4 and DIW 3D printed bulk g-C_3N_4/MC revealed significant piezoelectric properties, broadening their potential applications. Finally, the DLP 3D printed g-C_3N_4 composites were shown to have excellent sensitivity for the detection of a model heavy metal, Pb^{2+}, further enhancing their potential for applications in new areas, such as electrochemical sensors for other heavy metal ions.

The multifunctional properties and chemical stability of the 3D printed composites offer novel opportunities for the design of tailored systems and their deployment across diverse fields, including the chemical and pharmaceutical industries.

Author contributions

The manuscript was written through contributions of all authors. AM, DVS and VM designed and implemented the material synthesis and 3D printing procedures. KN and SK were responsible for photocatalytic and piezoelectric experiments and analysis while CI and MS performed and interpreted FTIR, UV-vis absorption as well as time-resolved photoluminescence measurements. ACK, AM and VM performed and interpreted the electrochemical measurements while AG performed PFM analysis. SK and VM provided supervision, review and funding acquisition. AM and VM were responsible for formatting and editing the final draft.

Conflicts of interest

There are no conflicts to declare.

Data availability

The data supporting this article have been included as part of the ESI.†

Acknowledgements

The authors would like to thank the European Union for funding AM's work within the Marie Skłodowska-Curie Actions (MSCA) doctoral network (GreenDigiPharma, No. 101073089) and DVS and VM (SusPharma, No. 101057430). The authors wish to acknowledge the University of Study of Bari for characterising the 3D printed materials and powders with UV-Vis absorbance spectroscopy, photoluminescence and time-resolved spectroscopy, and C2CAT.eu for providing a reference g-C_3N_4 powder. The authors would like to thank Zsófia Kovácska and Myrjam Mertens for their help with the XRD measurements, Nancy Dewit for SEM, Jan Jordens for DART-MS, Anne-Marie De Wilde for N_2 adsorption and Monika Kus for her assistance with the polymer precipitation process.

Notes and references

1 J. Xu, G. Wang, J. Fan, B. Liu, S. Cao and J. Yu, g-C_3N_4 modified TiO_2 nanosheets with enhanced photoelectric conversion efficiency in dye-sensitized solar cells, *J. Power Sources*, 2015, **274**, 77–84.

2 J. Xu, T. J. K. Brenner, L. Chabanne, D. Neher, M. Antonietti and M. Shalom, Liquid-Based Growth of Polymeric Carbon Nitride Layers and Their Use in a Mesostructured Polymer Solar Cell with Voc Exceeding 1 V, *J. Am. Chem. Soc.*, 2014, **136**, 13486–13489.

3 M. Ayán-Varela, S. Villar-Rodil, J. I. Paredes, J. M. Munuera, A. Pagán, A. A. Lozano-Pérez, J. L. Cenis, A. Martínez-Alonso and J. M. D. Tascón, Investigating the Dispersion Behavior in Solvents, Biocompatibility, and Use as Support for Highly Efficient Metal Catalysts of Exfoliated Graphitic Carbon Nitride, *ACS Appl. Mater. Interfaces*, 2015, **7**, 24032–24045.

4 M. Ismael and Y. Wu, A mini-review on the synthesis and structural modification of g-C_3N_4-based materials, and their applications in solar energy conversion and environmental remediation, *Sustainable Energy Fuels*, 2019, **3**, 2907–2925.
5 X. Wang, K. Maeda, A. Thomas, K. Takanabe, G. Xin, J. M. Carlsson, K. Domen and M. Antonietti, A metal-free polymeric photocatalyst for hydrogen production from water under visible light, *Nat. Mater.*, 2009, **8**, 76–80.
6 H. A. Bicalho, J. L. Lopez, I. Binatti, P. F. R. Batista, J. D. Ardisson, R. R. Resende and E. Lorençon, Facile synthesis of highly dispersed Fe(II)-doped g-C_3N_4 and its application in Fenton-like catalysis, *Mol. Catal.*, 2017, **435**, 156–165.
7 Y. Zhou, L. Zhang, J. Liu, X. Fan, B. Wang, M. Wang, W. Ren, J. Wang, M. Li and J. Shi, Brand new P-doped g-C_3N_4: enhanced photocatalytic activity for H2 evolution and Rhodamine B degradation under visible light, *J. Mater. Chem. A*, 2015, **3**, 3862–3867.
8 J. Jin, Q. Liang, C. Ding, Z. Li and S. Xu, Simultaneous synthesis-immobilization of Ag nanoparticles functionalized 2D g-C_3N_4 nanosheets with improved photocatalytic activity, *J. Alloys Compd.*, 2017, **691**, 763–771.
9 Y. Luo, Y. Zhu, Y. Han, H. Ye, R. Liu, Y. Lan, M. Xue, X. Xie, S. Yu, L. Zhang, Z. Yin and B. Gao, g-C_3N_4-based photocatalysts for organic pollutant removal: a critical review, *Carbon Res.*, 2023, **2**, 14.
10 G. Shi, L. Yang, Z. Liu, X. Chen, J. Zhou and Y. Yu, Photocatalytic reduction of CO2 to CO over copper decorated g-C_3N_4 nanosheets with enhanced yield and selectivity, *Appl. Surf. Sci.*, 2018, **427**, 1165–1173.
11 M. Li, L. Zhang, X. Fan, Y. Zhou, M. Wu and J. Shi, Highly selective CO2 photoreduction to CO over g-C_3N_4/Bi_2WO_6 composites under visible light, *J. Mater. Chem. A*, 2015, **3**, 5189–5196.
12 H. Gao, S. Yan, J. Wang, Y. A. Huang, P. Wang, Z. Li and Z. Zou, Towards efficient solar hydrogen production by intercalated carbon nitride photocatalyst, *Phys. Chem. Chem. Phys.*, 2013, **15**, 18077–18084.
13 J. Hong, X. Xia, Y. Wang and R. Xu, Mesoporous carbon nitride with in situ sulfur doping for enhanced photocatalytic hydrogen evolution from water under visible light, *J. Mater. Chem.*, 2012, **22**, 15006–15012.
14 A. Akhundi, A. Zaker Moshfegh, A. Habibi-Yangjeh and M. Sillanpää, Simultaneous Dual-Functional Photocatalysis by g-C_3N_4-Based Nanostructures, *ACS ES&T Eng.*, 2022, **2**, 564–585.
15 Y. Shao, C. Liu, H. Ma, J. Chen, C. Dong, D. Wang and Z. Mao, Piezocatalytic performance difference of graphitic carbon nitride (g-C_3N_4) derived from different precursors, *Chem. Phys. Lett.*, 2022, **801**, 139748.
16 T. Wu, Z. Liu, B. Shao, Q. He, Y. Pan, X. Zhang, J. Sun, M. He, L. Ge, C. Cheng and T. Hu, Enhanced piezo-photocatalytic degradation of organic pollutants by cambered wall lamellar structure of porous tubular g-C_3N_4, *Nano Energy*, 2024, **120**, 109137.
17 J. Lei, Y. Chen, F. Shen, L. Wang, Y. Liu and J. Zhang, Surface modification of TiO_2 with g-C_3N_4 for enhanced UV and visible photocatalytic activity, *J. Alloys Compd.*, 2015, **631**, 328–334.
18 F. Goettmann, A. Fischer, M. Antonietti and A. Thomas, Chemical Synthesis of Mesoporous Carbon Nitrides Using Hard Templates and Their Use as a Metal-Free Catalyst for Friedel–Crafts Reaction of Benzene, *Angew. Chem., Int. Ed.*, 2006, **45**, 4467–4471.
19 G. Liu, P. Niu, C. Sun, S. C. Smith, Z. Chen, G. Q. Lu and H.-M. Cheng, Unique Electronic Structure Induced High Photoreactivity of Sulfur-Doped Graphitic C_3N_4, *J. Am. Chem. Soc.*, 2010, **132**, 11642–11648.
20 J. Zhang, X. Chen, K. Takanabe, K. Maeda, K. Domen, J. D. Epping, X. Fu, M. Antonietti and X. Wang, Synthesis of a Carbon Nitride Structure for Visible-Light Catalysis by Copolymerization, *Angew. Chem., Int. Ed.*, 2010, **49**, 441–444.
21 M. Wu, J.-M. Yan, X.-W. Zhang and M. Zhao, Synthesis of g-C_3N_4 with heating acetic acid treated melamine and its photocatalytic activity for hydrogen evolution, *Appl. Surf. Sci.*, 2015, **354**, 196–200.
22 Q. Xiang, J. Yu and M. Jaroniec, Preparation and Enhanced Visible-Light Photocatalytic H2-Production Activity of Graphene/C_3N_4 Composites, *J. Phys. Chem. C*, 2011, **115**, 7355–7363.
23 G. Dong, K. Zhao and L. Zhang, Carbon self-doping induced high electronic conductivity and photoreactivity of g-C_3N_4, *Chem. Commun.*, 2012, **48**, 6178–6180.
24 F. Dong, M. Ou, Y. Jiang, S. Guo and Z. Wu, Efficient and Durable Visible Light Photocatalytic Performance of Porous Carbon Nitride Nanosheets for Air Purification, *Ind. Eng. Chem. Res.*, 2014, **53**, 2318–2330.
25 N. Chidhambaram and K. Ravichandran, Single step transformation of urea into metal-free g-C_3N_4 nanoflakes for visible light photocatalytic applications, *Mater. Lett.*, 2017, **207**, 44–48.
26 X. Li, H. Zhang, J. Huang, J. Luo, Z. Feng and X. Wang, Folded nano-porous graphene-like carbon nitride with significantly improved visible-light photocatalytic activity for dye degradation, *Ceram. Int.*, 2017, **43**, 15785–15792.
27 J. H. Thurston, N. M. Hunter, L. J. Wayment and K. A. Cornell, Urea-derived graphitic carbon nitride (u-g-C_3N_4) films with highly enhanced antimicrobial and sporicidal activity, *J. Colloid Interface Sci.*, 2017, **505**, 910–918.
28 L. Yang, X. Liu, Z. Liu, C. Wang, G. Liu, Q. Li and X. Feng, Enhanced photocatalytic activity of g-C_3N_4 2D nanosheets through thermal exfoliation using dicyandiamide as precursor, *Ceram. Int.*, 2018, **44**, 20613–20619.
29 S. Yang, Y. Gong, J. Zhang, L. Zhan, L. Ma, Z. Fang, R. Vajtai, X. Wang and P. M. Ajayan, Exfoliated Graphitic Carbon Nitride Nanosheets as Efficient Catalysts for Hydrogen Evolution Under Visible Light, *Adv. Mater.*, 2013, **25**, 2452–2456.
30 J. Ran, T. Y. Ma, G. Gao, X.-W. Du and S. Z. Qiao, Porous P-doped graphitic carbon nitride nanosheets for synergistically enhanced visible-light photocatalytic H2 production, *Energy Environ. Sci.*, 2015, **8**, 3708–3717.
31 J. Yan, X. Han, X. Zheng, J. Qian, J. Liu, X. Dong and F. Xi, One-step template/chemical blowing route to synthesize

flake-like porous carbon nitride photocatalyst, *Mater. Res. Bull.*, 2017, **94**, 423–427.

32 Y. Wang, H. Cai, F. Qian, Y. Li, J. Yu, X. Yang, M. Bao and X. Li, Facile one-step synthesis of onion-like carbon modified ultrathin g-C_3N_4 2D nanosheets with enhanced visible-light photocatalytic performance, *J. Colloid Interface Sci.*, 2019, **533**, 47–58.

33 N. Rono, J. K. Kibet, B. S. Martincigh and V. O. Nyamori, A comparative study between thermal etching and liquid exfoliation of bulk graphitic carbon nitride to nanosheets for the photocatalytic degradation of a model environmental pollutant, Rhodamine B, *J. Mater. Sci.: Mater. Electron.*, 2021, **32**, 687–706.

34 X. Wang, K. Maeda, X. Chen, K. Takanabe, K. Domen, Y. Hou, X. Fu and M. Antonietti, Polymer Semiconductors for Artificial Photosynthesis: Hydrogen Evolution by Mesoporous Graphitic Carbon Nitride with Visible Light, *J. Am. Chem. Soc.*, 2009, **131**, 1680–1681.

35 Y.-H. Son, M. park, Y. B. Choy, H. R. Choi, D. S. Kim, K. C. Park and J.-H. Choy, One-pot synthetic route to polymer–silica assembled capsule encased with nonionic drug molecule, *Chem. Commun.*, 2007, 2799–2801, DOI: 10.1039/B702288C,.

36 Y.-H. Son, M. Park, S. T. Kim and J.-H. Choy, Mixed Micelle-Template Route to Mesoporous Silica, *J. Nanosci. Nanotechnol.*, 2007, **7**, 3819–3822.

37 Y. Fukasawa, K. Takanabe, A. Shimojima, M. Antonietti, K. Domen and T. Okubo, Synthesis of Ordered Porous Graphitic-C_3N_4 and Regularly Arranged Ta_3N_5 Nanoparticles by Using Self-Assembled Silica Nanospheres as a Primary Template, *Chem. – Asian J.*, 2011, **6**, 103–109.

38 J.-H. Yang, G. Kim, K. Domen and J.-H. Choy, Tailoring the Mesoporous Texture of Graphitic Carbon Nitride, *J. Nanosci. Nanotechnol.*, 2013, **13**, 7487–7492.

39 M. R. Gogate, New Paradigms and Future Critical Directions in Heterogeneous Catalysis and Multifunctional Reactors, *Chem. Eng. Commun.*, 2017, **204**, 1–27.

40 M. N. Nadagouda, M. Ginn and V. Rastogi, A review of 3D printing techniques for environmental applications, *Curr. Opin. Chem. Eng.*, 2020, **28**, 173–178.

41 L. R. S. Rosseau, V. Middelkoop, H. A. M. Willemsen, I. Roghair and M. van Sint Annaland, Review on Additive Manufacturing of Catalysts and Sorbents and the Potential for Process Intensification, *Front. Chem. Eng.*, 2022, **4**, 1.

42 J. M. Aguirre-Cortés, A. I. Moral-Rodríguez, E. Bailón-García, A. Davó-Quiñonero, A. F. Pérez-Cadenas and F. Carrasco-Marín, 3D printing in photocatalysis: Methods and capabilities for the improved performance, *Appl. Mater. Today*, 2023, **32**, 101831.

43 X. Liu, S. Ma, H. Yang, P. He, X. Duan, D. Jia, P. Colombo and Y. Zhou, 3D-printed green and low-cost porous g-C_3N_4/geopolymer components for the removal of methylene blue from wastewater, *J. Am. Ceram. Soc.*, 2024, **107**, 3068–3082.

44 J. Luo, V. Ruta, I. S. Kwon, J. Albertazzi, N. Allasia, O. Nevskyi, V. Busini, D. Moscatelli and G. Vilé, Fabricating a Structured Single-Atom Catalyst via High-Resolution Photopolymerization 3D Printing, *Adv. Funct. Mater.*, 2024, **34**, 2404794.

45 I.-A. Baragau, J. Buckeridge, K. G. Nguyen, T. Heil, M. T. Sajjad, S. A. J. Thomson, A. Rennie, D. J. Morgan, N. P. Power, S. A. Nicolae, M.-M. Titirici, S. Dunn and S. Kellici, Outstanding visible light photocatalysis using nano-TiO_2 hybrids with nitrogen-doped carbon quantum dots and/or reduced graphene oxide, *J. Mater. Chem. A*, 2023, **11**, 9791–9806.

46 B.-w Sun, H.-y Yu, Y.-j Yang, H. Li, C. Zhai, D.-j Qian and M. Chen, New complete assignment of X-ray powder diffraction patterns in graphitic carbon nitride using discrete Fourier transform and direct experimental evidence, *Phys. Chem. Chem. Phys.*, 2017, **19**(38), 26072–26084.

47 C. Fan, Q. Feng, G. Xu, J. Lv, Y. Zhang, J. Liu, Y. Qin and Y. Wu, Enhanced photocatalytic performances of ultrafine g-C_3N_4 nanosheets obtained by gaseous stripping with wet nitrogen, *Appl. Surf. Sci.*, 2018, **427**, 730–738.

48 S. Ganesan, T. Kokulnathan, S. Sumathi and A. Palaniappan, Efficient photocatalytic degradation of textile dye pollutants using thermally exfoliated graphitic carbon nitride (TE–g–C_3N_4), *Sci. Rep.*, 2024, **14**, 2284.

49 L. Kong, J. Wang, X. Mu, R. Li, X. Li, X. Fan, P. Song, F. Ma and M. Sun, Porous size dependent g-C_3N_4 for efficient photocatalysts: Regulation synthesizes and physical mechanism, *Mater. Today Energy*, 2019, **13**, 11–21.

50 B. L. Phoon, C. W. Lai, G.-T. Pan, T. C. K. Yang and J. C. Juan, Highly Mesoporous g-C_3N_4 with Uniform Pore Size Distribution via the Template-Free Method to Enhanced Solar-Driven Tetracycline Degradation, *Nanomaterials*, 2021, **11**, 2041.

51 P. Niu, L. Zhang, G. Liu and H.-M. Cheng, Graphene-Like Carbon Nitride Nanosheets for Improved Photocatalytic Activities, *Adv. Funct. Mater.*, 2012, **22**, 4763–4770.

52 B. Zhu, P. Xia, W. Ho and J. Yu, Isoelectric point and adsorption activity of porous g-C_3N_4, *Appl. Surf. Sci.*, 2015, **344**, 188–195.

53 I. Papailias, N. Todorova, T. Giannakopoulou, N. Ioannidis, N. Boukos, C. P. Athanasekou, D. Dimotikali and C. Trapalis, Chemical vs thermal exfoliation of g-C_3N_4 for NOx removal under visible light irradiation, *Appl. Catal., B*, 2018, **239**, 16–26.

54 Y. Yuan, L. Zhang, J. Xing, M. I. B. Utama, X. Lu, K. Du, Y. Li, X. Hu, S. Wang, A. Genç, R. Dunin-Borkowski, J. Arbiol and Q. Xiong, High-yield synthesis and optical properties of g-C_3N_4, *Nanoscale*, 2015, **7**, 12343–12350.

55 Z. Limpouchová and K. Procházka, in *Fluorescence Studies of Polymer Containing Systems*, ed. K. Procházka, Springer International Publishing, Cham, 2016, pp. 91–149, DOI: 10.1007/978-3-319-26788-3_4.

56 A. Iborra-Torres, M. Huš, K. Nguyen, A. Vamvakeros, M. T. Sajjad, S. Dunn, M. Mertens, S. Jacques, A. M. Beale, B. Likozar, G. Hyett, S. Kellici and V. Middelkoop, 3D printed SrNbO2N photocatalyst for degradation of organic pollutants in water, *Mater. Adv.*, 2023, **4**, 3461–3472.

57 M. Gouamid, M. R. Ouahrani and M. B. Bensaci, Adsorption Equilibrium, Kinetics and Thermodynamics of Methylene

Blue from Aqueous Solutions using Date Palm Leaves, *Energy Procedia*, 2013, **36**, 898–907.

58 Y. Xu, Q. Guo, L. Huang, H. Feng, C. Zhang, H. Xu and M. Wang, Toward Efficient Preconcentrating Photocatalysis: 3D g-C_3N_4 Monolith with Isotype Heterojunctions Assembled from Hybrid 1D and 2D Nanoblocks, *ACS Appl. Mater. Interfaces*, 2019, **11**, 31934–31942.

59 D. Cao, X. Wang, H. Zhang, D. Yang, Z. Yin, Z. Liu, C. Lu and F. Guo, Rational Design of Monolithic g-C(3)N(4) with Floating Network Porous-like Sponge Monolithic Structure for Boosting Photocatalytic Degradation of Tetracycline under Simulated and Natural Sunlight Illumination, *Molecules*, 2023, **28**, 3989.

60 P. He, X. Tang, L. Chen, P. Xie, L. He, H. Zhou, D. Zhang and T. Fan, Patterned Carbon Nitride–Based Hybrid Aerogel Membranes via 3D Printing for Broadband Solar Wastewater Remediation, *Adv. Funct. Mater.*, 2018, **28**, 1801121.

61 A. Ali, M. Amin, M. Tahir, S. S. Ali, A. Hussain, I. Ahmad, A. Mahmood, M. U. Farooq and M. A. Farid, g-C_3N_4/Fe_3O_4 composites synthesized via solid-state reaction and photocatalytic activity evaluation of methyl blue degradation under visible light irradiation, *Front. Mater.*, 2023, **10**, 1.

62 L. Li, J. Li, H. Luo, S. Li and J. Yang, Physicochemical and Photocatalytic Properties of 3D-Printed TiO_2/Chitin/Cellulose Composite with Ordered Porous Structures, *Polymers*, 2022, **14**, 5435.

63 L. Hernández-Afonso, R. Fernández-González, P. Esparza, M. E. Borges, S. Díaz González, J. Canales-Vázquez and J. C. Ruiz-Morales, Ceramic-Based 3D Printed Supports for Photocatalytic Treatment of Wastewater, *J. Chem.*, 2017, **2017**, 7602985.

64 S. Güler, Mechanical, Thermal, and Photocatalytic Properties of TiO_2/ZnO Hybrid Composites Fabricated via Additive Manufacturing, *Recep Tayyip Erdogan Univ. J. Sci. Eng.*, 2024, **5**, 149–158.

65 K. Wang, L. Yu, S. Yin, H. Li and H. Li, Photocatalytic degradation of methylene blue on magnetically separable FePc/Fe_3O_4 nanocomposite under visible irradiation, *Pure Appl. Chem.*, 2009, **81**, 2327–2335.

66 P. Kumar, N. S. Alsaiari, A. Gaur, D. Karan, R. Vaish, A. Amari, H. Osman, Y. H. Joo, T. H. Sung, A. Kumar and W.-C. Liu, Degradation of dye through mechano-catalysis using $BaBi_4Ti_4O_{15}$ catalyst, *Sci. Rep.*, 2024, **14**, 18177.

67 A. Gaur, V. S. Chauhan and R. Vaish, Planetary ball milling induced piezocatalysis for dye degradation using $BaTiO_3$ ceramics, *Environ. Sci.: Adv.*, 2023, **2**, 462–472.

68 M. Kumar, R. Vaish, I. Kebaili, I. Boukhris, H. Kwang Benno Park, Y. Hwan Joo, T. Hyun Sung and A. Kumar, Ball-milling synthesized $Bi_2VO_{5.5}$ for piezo-photocatalytic assessment, *Sci. Rep.*, 2023, **13**, 8188.

69 S. Wang, S. Tang, H. Yang, F. Wang, C. Yu, H. Gao, L. Fang, G. Sun, Z. Yi and D. Li, A novel heterojunction ZnO/CuO piezoelectric catalysts: fabrication, optical properties and piezoelectric catalytic activity for efficient degradation of methylene blue, *J. Mater. Sci.: Mater. Electron.*, 2022, **33**, 7172–7190.

70 W. Wang, J. Zhao, Y. Sun and H. Zhang, Facile synthesis of g-C_3N_4 with various morphologies for application in electrochemical detection, *RSC Adv.*, 2019, **9**, 7737–7746.

71 M. R. Mahmoudian, W. J. Basirun, Y. Alias and P. MengWoi, Investigating the effectiveness of g-C_3N_4 on Pt/g-C_3N_4/polythiophene nanocomposites performance as an electrochemical sensor for Hg^{2+} detection, *J. Environ. Chem. Eng.*, 2020, **8**, 104204.